Total elastic scattering cross sections for metastable argon on xenon

J. Li,* M. Faxas, J. W. Sheldon, and K. A. Hardy
Physics Department, Florida International University, University Park, Miami, Florida 33199
(Received 7 October 1993)

The interaction potential between metastable argon (Ar^*) and xenon has been determined by a measurement of the velocity dependence of the total elastic-scattering cross section for the reaction Ar^*+Xe. The cross sections have been corrected for the inelastic contribution to the reaction. The potential parameters have been determined by comparing the data with potential parameters calculated with both semiclassical and full quantum calculations of the cross sections. The semiclassical computation resulted in a potential with a well depth of 18 meV and a position of 4.6 Å while the full quantum yielded a well depth of 25.4 meV and a position of 4.3 Å.

PACS number(s): 34.40.+n, 34.20.Cf

I. INTRODUCTION

The interaction between metastable argon, Ar^* ($Ar\ ^3P_{2,0}$), and xenon has been the subject of several studies over the last 20 years using both differential- and integral-scattering cross-section measurements. Surprisingly, there is still not satisfactory agreement between the experimental results from several laboratories, and therefore the potential describing this reaction is not satisfactorily determined. The need for a better description of the Ar^*+Xe potential was recently pointed out in studies by Mueller, Zimmerman, and Krenos [1], who are studying the quenching of Ar^* by xenon. The Ar^*+Xe reaction has been studied by authors including Martin *et al.*, who used differential-scattering cross-section measurements [2], Nenner, who used integral-scattering cross-section measurements in a scattering cell with a supersonic beam source [3], and Kerstel *et al.*, who used integral-scattering cross-section measurements in a crossed-beam configuration [4]. As a measure of the disagreement between potentials used to describe this reaction, if the attractive term in the potential is described by just an induced dipole or van der Waals attractive term $-C_6/r^6$, the values for the C_6 term derived from experimental results vary by nearly a factor of 2 and the disagreement between the attractive term used to compare the Ar^*+Xe reaction and its analog the $K+Xe$ reaction is even worse [5]. The values predicted by theoretical calculations for the C_6 term lie between the extremes of the experimental measurements [6,7]. We have measured the absolute integral-scattering cross section for the reaction Ar^*+Xe in an effort to resolve the apparent discrepancy between the several experimental measurements and to better determine the parameters of the potential describing this reaction.

*Present address: Florida State University, Physics Department, Tallahassee, FL 32306.

II. APPARATUS

The time-of-flight molecular-beam apparatus used in these measurements has been described in detail elsewhere [8–11]. The metastable atoms are created in a direct current discharge and velocity analyzed by a chopper wheel and time-of-flight analysis. The elastic-scattering cross sections are determined from measurements of attenuation of the well-collimated Ar^* beam in a Xe gas target cell. The time-of-flight technique allows the use of all velocities present in the argon discharge for the scattering measurement and all velocities are sampled simultaneously. Figure 1 is a schematic diagram of the apparatus, which consists of two coupled vacuum chambers pumped by two independent pumping systems. One of the vacuum chambers contains the source and the second chamber contains the scattering cell and the detector system. The source chamber is typically held at a pressure of about 1×10^{-5} Torr while the chamber containing the scattering cell and the detector are held at a pressure of about 2×10^{-6} Torr during an experimental run. The metastable atom source is an effusive source producing metastable atoms, ions, and Rydberg atoms in a Penning discharge. The discharge is maintained in a Pyrex tube about 3.1 cm long between a thoria-coated tungsten ribbon and the anode containing a 9.5-mm×0.2-mm exit slit through which the product atoms of the discharge effuse. A potential of approximately 50 V between the cathode and anode maintains a discharge current of about 260 ma. The discharge current is kept constant by the adjustment of the filament temperature. The pressure in the source is maintained at a preset value of between 35 and 60 mTorr by an automatic pressure controller controlling the flow of research grade argon to the discharge. The source produces argon atoms in a mixture of the $^3P_{2,0}$ metastable states and no state separation was used in these experiments; however, other measurements on a similar source indicate that the $^3P_2$ state dominates the $^3P_0$ state by about the statistically expected ratio of 6 to 1 [12].

The rotary beam chopper is located just past the exit slit of the source. The 5.8-cm-diam chopper wheel has

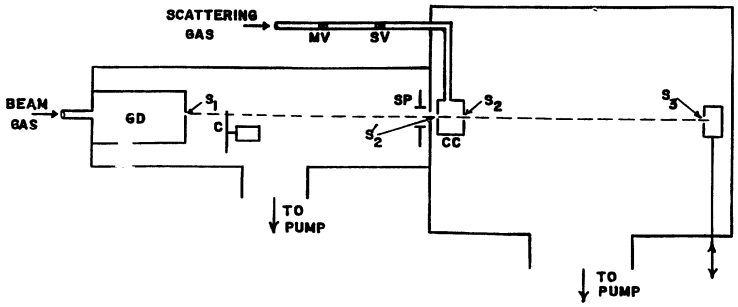

FIG. 1. The apparatus. GD denotes the gas discharge, C the chopper, SP the sweep plates, CC the collision cell, MV the metering valve, SV the solenoid valve and S1,S2',S2,S3 the beam defining slits.

two opposing slits 0.75 mm in width and is driven by a synchronous motor at 60 Hz. The resulting velocity resolution is a function of velocity and varies from 1.2% at a velocity of 500 m/sec to 38% at a velocity of 5500 m/sec. The beam then passes through a set of sweep plates providing a 500-V/cm electric field across the beam path that removes any Rydberg states and charged particles.

The scattering cell is equipped with entrance and exit slits 0.2 mm in width. The cell is 34.9 mm long. The scattering cell has separate ports for pressure measurement and for the introduction of the scattering gas into the scattering cell. The scattering gas handling system consists of a small reservoir kept at a constant pressure by the scattering gas pressure regulator, an electrically operated metering valve which is manually controlled, and a computer controlled solenoid valve. The metering valve regulates the flow of scattering gas into the scattering cell when the solenoid valve is open, and consequently controls the scattering gas pressure. When the solenoid valve is closed, the scattering cell is evacuated through the entrance and exit slits.

The accuracy of an absolute-scattering cross-section measurement depends directly on the accuracy of the measurement of the pressure in the scattering gas cell. Consequently, in these measurements two independent pressure measurement systems are used; the calibration of one of these systems is traceable to NIST standards. The electronic capacitance manometer systems used are a Datametrics Model 1014A whose output is digitized and recorded at the beginning and end of each gas-in–gas-out cycle along with the time-of-flight data by the data-acquisition computer. The output of a MKS model 390 electronic capacitance manometer was manually recorded for comparison throughout the data-acquisition process. A small pressure correction (1.7%) was made to the measured pressures due to the temperature difference between the sensing unit of the capacitance manometer and the collision cell [13].

The 9.5-mm×0.28-mm entrance slit to the detector system is located 73 cm from the rotary beam chopper. The angular resolution for this beam geometry is 1.8′ by the Kusch criterion [14]. After passing the entrance slit to the detector system the particles impinge on a tungsten catcher plate where the metastable atoms eject Auger electrons, which then are captured by a channeltron electron multiplier. The only particles left in the atom beam after passing the sweep plates are ground-state and metastable-state atoms. As the kinetic energy of a ground-state atom is insufficient to eject an Auger electron, the system is sensitive only to metastable atoms.

III. RESULTS

The data used in this measurement were accumulated in 30 separate data-acquisition sessions with a total data-acquisition time of 476 h. The scattering cell pressures used in these sessions varied between 0.08 mTorr and 0.14 mTorr. The data from each run were analyzed separately and the results of these runs averaged to give the data used in the measurement. This procedure was used to eliminate any random error in the pressure measurement. A data-acquisition run was broken into eight-min cycles in the following manner. One minute was used to stabilize the pressure in the scattering cell, 3 min for counting with gas in the collision cell, 1 min to evacuate the collision cell, and 3 min for counting with gas out of the collision cell. At the beginning of each gas-in–gas-out cycle, the pressure in the collision cell was recorded by the data-acquisition computer along with the time-of-flight data. Before the data from a particular cycle were added to the data already acquired in a particular run, the computer monitored the beam intensity, and if this intensity was not within prescribed limits, the run was stopped before the new data were added to the previously acquired data. This procedure was used to average out the effects of small changes in beam intensity during a counting cycle.

A typical set of time-of-flight data is shown in Fig. 2. The data show the time-of-flight data from a Maxwellian velocity distribution and a fast peak, due to dissociative recombination reactions in the discharge [15]. The use of the fast peak of metastable atoms allows the extension of the useful velocity range to about 5000 m/sec. The beam velocities were calculated from $V_b = L_p/t$, where the flight path L_p was 73 cm. The intensity distributions for gas in the scattering cell $I_i(t)$ and for gas out of the scattering cell $I_0(t)$ with the background subtracted were used to compute the effective total cross sections $Q(V_b)$ with the expression

$$Q(V_b) = [kT/PL]\ln\{I_0(t)/I_i(t)\} , \quad (1)$$

where k is Boltzmann's constant, P is the collision cell pressure, T the collision cell temperature, and L the collision cell length. Single-collision conditions were verified for the range of scattering gas pressures used in these ex-

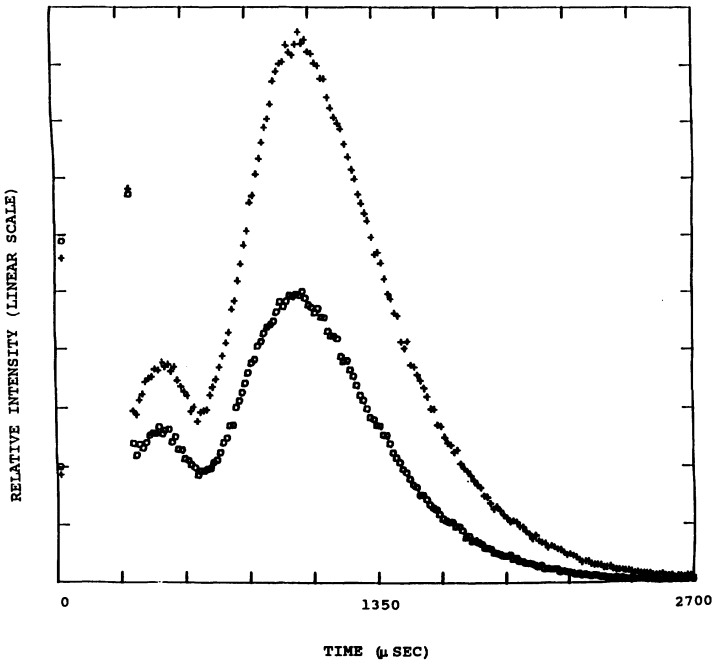

FIG. 2. A typical set of gas-in–gas-out time-of-flight data. The crosses represent gas out of the collision cell, while the squares represent gas in the collision cell. The horizontal axis is flight time in microseconds while the vertical axis corresponds to beam intensity. Each channel has a width of 11.9 μsecs. The initial photon peak is off scale. A small background has been subtracted in these data.

periments by plotting the right-hand side of Eq. (1) versus collision cell pressure and noting that the total cross section is pressure independent for velocities in the Maxwellian range. The relative velocity (g) -dependent apparent total scattering cross section $Q_a(g)$ can be calculated from $Q(V_b)$ and is corrected for the motion of the target gas. Using the procedure of Lang, Lilenfield, and Kinsey [16], the apparent total cross section as a function of the relative velocity averaged over the velocity distribution of the target gas is

$$Q_a(\bar{g})=\{V_b Q(V_b)\}/[\bar{g}f(s,x)] , \tag{2}$$

where $x=V_b/V_p$ and V_p is the most probable velocity of xenon in the target cell. A tabulation of the function $f(s,x)$ is given by Lang, Lilenfield, and Kinsey [16] and assumes that the long-range attractive part of the potential varies as $1/r^s$. The function is nearly independent of s for $4\leq s\leq 18$ and only differs from unity by about 3% for our experimental conditions. In order to correct for the attenuation of the beam due to inelastic scattering, the data of Krenos were found to be well represented by the empirical function

$$Q_i(\bar{g})=[81/(\bar{g}-300)^{0.4}+40]\ \text{Å}^2 \tag{3}$$

for $\bar{g}>400$ m/sec. In the expression above, $\bar{g}$ is the averaged relative velocity of the collision partners.

The finite angular resolution of the apparatus reduces the measured cross section. von Busch [17] has derived a correction for this effect. The correction in the form given by von Busch [17] is

$$\Delta Q/Q_e=0.066\,46Q_e^{1/2}\gamma k(1+0.374X^{-2}) , \tag{4}$$

where $k=m_b V_b/\hbar$ is the wave number of the beam and $\gamma=F\Theta_r$. The F factor depends on the width of the beam relative to the detector acceptance angle, and is given in tables by von Busch as 4.0 for our geometry. In this expression Θ_r is the detector acceptance angle. X is the ratio of the beam velocity to the most probable velocity of the target gas. This can be rewritten in terms of the apparent total scattering cross section $Q_a(\bar{g})$ using $Q_e=Q_a+\Delta Q$ to give the correction as

$$\Delta Q=\alpha Q_a^{3/2}/[1-(\tfrac{3}{2})\alpha Q_a^{1/2}] , \tag{5a}$$

where

$$\alpha=0.066\,46k\gamma(1+0.374X^{-2}) . \tag{5b}$$

This equation does not require iteration to find the correction, as does the original expression. We have used this result to correct our data with the expression

$$Q_e(\bar{g})=Q(\bar{g})+\Delta Q(\bar{g})-Q_i(\bar{g}) . \tag{6}$$

IV. DISCUSSION

We have analyzed our data using both the semiclassical model of Kerstel *et al.* [4] and a full quantum calculation of the phase shifts. The data were fitted to the semiclassical model function

$$Q=Q_a+Q_{gl} , \tag{7a}$$

$$Q_a=A_1X^{A_2} , \tag{7b}$$

$$Q_{gl}=A_{gl}\sin(\theta_{gl}) , \tag{7c}$$

$$A_{gl}=A_3X^{-1/2}+A_4X^{3/2} , \tag{7d}$$

$$\theta_{gl}=A_5+A_6X+A_7X^3 . \tag{7e}$$

The inverse relative velocity is $X=1000/\bar{g}$. The A_i are the free parameters in the nonlinear least-squares-fitting procedure. The parameters giving the best fit are given in Table I.

TABLE I. The results of the semiclassical data analysis.

Parameter	Value A_2 free	Value A_2 fixed at 0.4
A_1	622.24±0.47 Å^2	621.14±0.47 Å^2
A_2	0.422±0.2	0.4
A_3	−17.26±0.53 Å^2	−14.27±0.51 Å^2
A_4	7.6±0.3 Å^2	4.30±0.49 Å^2
A_5	−2.85±8.3	−1.38±7.3
A_6	22.90±4.8	16.65±3.34
A_7	−2.23±3.8	7.05±3.6
C_s	$s=5.74$	$s=6$
	2.08×10^{-74} J m^6	5.4×10^{-77} J m^6
R_m	4.7 Å	4.6 Å
ε	15 meV	18 meV

In this model expression for the cross section, Q_a is the Landau-Lifshitz cross section [18]. A_2 can be used to deduce the long-range dependence of the potential $1/r^s$, where $s=(2/A_2)+1$. Using our value for A_2 we find $s=5.74$ for the long-range attractive part of the potential function. The Landau-Lifshitz cross section is then given as

$$Q_{\rm LL}=8.3105[C_s/(\hbar\bar{g})]^{0.422} \quad (8)$$

for a long-range attractive potential of the form $C_s r^{-s}$, where the C_s is the effective constant. Using the A_1 and A_2 constants from the fit we find $C_{5.74}=2.08\times10^{-74}$ J m^6. The semiclassical model was also used to determine the value of the constants when the value of A_2 was restricted to a value of 0.4 which corresponds to $s=6$. The χ^2 per degree of freedom was slightly worse for this fit. The expression

$$Q_{\rm LL}=8.083[C_6/(\hbar g)]^{0.4} \quad (9)$$

then gives $C_6=5.46\times10^{-77}$ J m^6, when a pure r^{-6} potential is assumed. The remainder of the parameters for the model function for the case of A_2 being restricted to 0.4 are also shown in Table I. Following Bernstein [18] we may calculate a potential depth and position of the minimum using the extrema in the cross section (found with θ_{gl} from the fit) and find $r_m=4.6$ Å and a well depth of 18 meV. The data and the fit to the data using the semiclassical model function with A_2 equal to 0.4 are shown in Fig. 3.

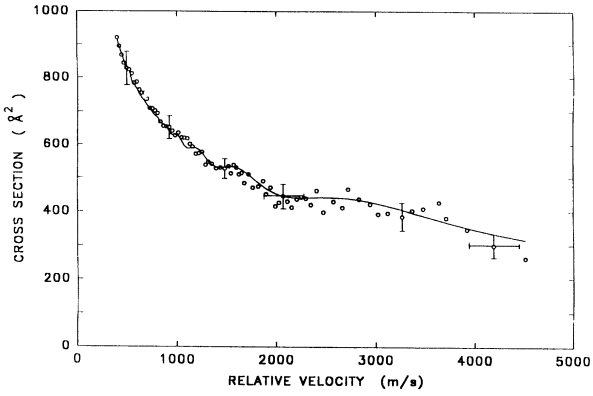

FIG. 3. The data and a fit to the data using the semiclassical model function described in the text with the long-range attractive potential term proportional to $1/r^6$. Typical error bars are shown with the data.

A second least-squares-fitting procedure was performed using a full quantum calculation to establish the theoretical data points. The parameters used as a starting point for the calculation were the potential parameters used to describe the Ar*+Kr interaction [11]. The full quantum calculation allows additional freedom in the choice of the potential used to fit the data. A quantum calculation of the phase shifts using the Numerov algorithm [18,19] to integrate the Schrödinger equation was used to calculate the cross sections. The integration started within the hard core of the potential and continued until the phase shifts satisfied a convergence criteria of less than a 0.1% change in the phase shift (Fig. 4).

TABLE II. The results of the full quantum phase-shift calculation. The potential used is $V(r)=V_{\rm HC}(r)-C_6/r^6-C_8/r^8-C_{10}/r^{10}$, where $V_{\rm HC}(r)=(A/r)^C$ when $r<B$ and $(B/r)^D(A/B)^C$ when $r\geq B$. All values in atomic units (except as noted).

Parameter	Value
A	5.104±0.09
B	7.55±0.36
C	14.50±0.11
D	10.09±0.48
C_{10}	13 794±662
C_8	2 900±55
C_6	615.2±11.6
C_6	(5.87±0.11)$\times10^{-77}$ J m^6
R_m	4.3 Å
ε	25.44 meV

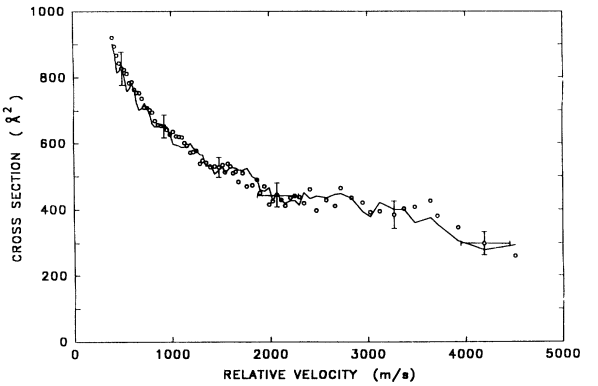

FIG. 4. The data and a fit to the data using a full quantum phase-shift calculation. Typical error bars are shown with the data points. The theoretical function was calculated at each of the data points and the line in the figure connects these theoretical points. We estimate an uncertainty of approximately 2% in the theoretical calculation due to the uncertainty of calculating high orders of the spherical Bessel functions.

TABLE III. A comparison of this work and other works referred to in the text. The units are atomic units unless otherwise specified.

	This work		Theory [6]	Expt.	
	Quantum fit	Semiclassical fit ($s=0.4$)		Ref. [3]	Ref. [4]
C_6	615	571.8	641	513	788
C_8	2 900		458 70		
C_{10}	13 794		427 300		
R_m	4.3 Å	4.6 Å		5.7 Å	5.4 Å
ε	25.4 meV	18 meV		4.4 meV	12.7 meV

Martin *et al.* [2] studied the Ar*+Xe system by measuring the angular distributions of Ar* scattered from xenon. They observed a broad "bump" in the angular distribution at 40° that they attribute to a kink in the wall of the hard core of the potential. A similar feature was observed in their studies of the Ar*+Kr reaction. Following the work of Martin [2], in our studies of the Ar*+Kr reaction [11] we used a potential with a kink in the hard core that gave the best fit to our Ar*+Kr data. We have used a similar potential in this work. The potential has the form

$$V(r)=V_{\rm HC}(r)-C_6/r^6-C_8/r^8-C_{10}/r^{10}\ , \qquad (10a)$$

where

$$V_{\rm HC}(r)=(A/r)^C$$

$$\text{when } r<B\ ,\ (B/r)^D(A/B)^C \text{ when } r\geq B\ . \qquad (10b)$$

The parameters of this potential that gave the best fit to the data are shown in Table II. The table also shows the potential-well position and well depth.

V. CONCLUSION

We have measured the absolute total elastic-scattering cross section for the reaction Ar* on Xe and from these data determined the interaction potential. We have analyzed the data with both the semiclassical approximation and a full quantum partial-wave analysis of the cross section. We believe that the best determination of the potential is given by the full quantum calculation, the results of which are shown in Table II. The disagreement between the well depth given by the semiclassical analysis and that given by the full quantum calculation illustrates the inadequacy of the model function in this case. The determination of the well depth from the semiclassical model relies on the accurate determination of the positions of the extrema in the phase function. A scattering cell measurement allows precise determination of the magnitude of the cross section, but is not as precise in the determination of the positions of the extrema in the cross section due to the lower velocity resolution as compared to a cross-beam measurement. Our data are in good agreement with the data of Nenner [3], but not in agreement with the well-resolved data of Kerstel *et al.* [4]. The disagreement with their data for the Ar*+Xe measurement was also evident in our measurement of the cross section for the Ar*+Kr [11] system. A comparison of the cross sections at 1000 m/sec shows that the data of Kerstel *et al.* were 1.28 times as large as our data for the case of Ar*+Kr and 1.21 times as large in the case of Ar*+Xe. Nenner [3] gives no easy way to compare his data at a particular velocity; however, a plot of our data and those of Nenner [3] shows good agreement. A comparison of the potential data from this work, from Nenner [3], from Kerstel *et al.* [4] and from the theoretical calculations of Proctor and Stwalley [6] is shown in Table III. Proctor's calculations are for the system K+Xe which is the analog of the Ar*+Xe system. The agreement for the value of C_6 is surprisingly good. The computed values for C_8 and C_{10} are not in agreement with the theory but these constants make small contributions to the potential in either case.

ACKNOWLEDGMENTS

J.W.S. and K.A.H. received partial support for this work through AFOSR Grant No. F49620-93-1-0159DEF.

[1] D. Mueller, A. Zimmerman, and J. Krenos (unpublished).
[2] D. W. Martin, T. Fukuyama, R. W. Gregor, R. M. Jordan, and P. E. Siska, J. Chem. Phys. **65**, 3720 (1976).
[3] T. Nenner, Entropie **42**, 142 (1971).
[4] E. R. T. Kerstel, C. P. J. W. Van Kruysdijk, J. C. Vlugter, and H. C. W. Beijerinck, Chem. Phys. **121**, 211 (1988).
[5] R. Helbing and H. Pauly, Z. Phys. **179**, 16 (1964).
[6] T. R. Proctor and W. C. Stwalley, J. Chem. Phys. **66**, 2063 (1977).
[7] A. Delgarno, Adv. Chem. Phys. **12**, 143 (1967).
[8] K. A. Hardy and J. W. Sheldon, Rev. Sci. Instrum. **52**, 1802 (1981).
[9] J. W. Sheldon and K. A. Hardy, Phys. Lett. **98A**, 332 (1983).
[10] K. A. Hardy and J. W. Sheldon, Phys. Rev. A **30**, 2761 (1984).

[11] H. Li, E. S. Gillman, J. W. Sheldon, and K. A. Hardy, Phys. Rev. A **45**, 225 (1992).
[12] M. E. Gersh, G. D. Sides, S. Y. Tang, and E. E. Muschlitz, Jr., J. Appl. Phys. **44**, 5356 (1973).
[13] G. Loriot and T. Moran, Rev. Sci. Instrum. **46**, 140 (1975).
[14] P. Kusch, J. Chem. Phys. **40**, 1 (1964).
[15] K. A. Hardy, E. Gillman, and J. W. Sheldon, J. Appl. Phys. **67**, 7240 (1990).
[16] N. C. Lang, H. V. Lilenfield, and J. L. Kinsey, J. Chem. Phys. **55**, 3114 (1971).
[17] F. von Busch, Z. Phys. **208**, 390 (1968).
[18] R. B. Bernstein, in *Molecular Beams,* edited by J. Ross (Wiley, New York, 1966).
[19] R. J. Munn, E. A. Maison, and F. J. Smith, J. Chem. Phys. **41**, 3978 (1964).